PCCP

ROYAL SOCIETY OF CHEMISTRY

PAPER

View Article Online
View Journal | View Issue

Cite this: *Phys. Chem. Chem. Phys.*, 2021, **23**, 26501

Intense chiral signal from α-helical poly-L-alanine observed in low-frequency Raman optical activity†

Shigeki Yamamoto, *[a] Shota Ishiro,[a] Jiří Kessler[b] and Petr Bouř *[b]

Raman optical activity (ROA) spectral features reliably indicate the structure of peptides and proteins, but the signal is often weak. However, we observed significantly enhanced low-frequency bands for α-helical poly-L-alanine (PLA) in solution. The biggest ROA signal at ~100 cm^{-1} is about 10 times stronger than higher-frequency bands described previously, which facilitates the detection. The low-frequency bands of PLA were compared to those of α-helical proteins. For PLA, density functional simulations well reproduced the experimental spectra and revealed that about 12 alanine residues within two turns of the α-helix generate the strong ROA band. Averaging based on molecular dynamics (MD) provided an even more realistic spectrum compared to the static model. The low-frequency bands could be largely related to a collective motion of the α-helical backbone, partially modulated by the solvent. Helical and intermolecular vibrational coordinates have been introduced and the helical unwinding modes were assigned to the strongest ROA signal at 101–128 cm^{-1}. Further analysis indicated that the helically arranged amide and methyl groups are important for the strong chiral signal of PLA, while the local chiral centers $C_\alpha H$ contribute in a minor way only. The strong low-frequency ROA can thus provide precious information about the motions of the peptide backbone and facilitate future protein studies.

Received 25th September 2021,
Accepted 5th November 2021

DOI: 10.1039/d1cp04401j

rsc.li/pccp

Introduction

Vibrational spectroscopy was established as a fast and flexible tool for analyzing molecular structure. The vibrational optical activity (VOA) techniques utilizing circularly polarized light provide additional sensitivity to the chiral structure and are conveniently used to study biologically related molecules such as proteins.[1,2] Traditionally, VOA comprises vibrational circular dichroism (VCD) and Raman optical activity (ROA), and has been applied to small molecules as well as to nucleic acids, proteins, carbohydrates, and even whole viruses.[3–8] Since the discovery in the 1970s,[9,10] the sensitivity and application range of the VOA methods have significantly improved. More complex applications appeared, such as experiments utilizing surface-enhancement[11,12] or chirality transfer[18] phenomena for boosting the sensitivity. However, despite the instrumental developments,[13–17] many VOA experiments for biological samples still require tens of hours and high concentrations/sample amounts. Thus the signal enhancement, such as the low-frequency VOA described here, significantly broadens the application field of the technique.

Unlike VCD, ROA in principle comprises a wide vibrational range, containing all fundamental molecular transitions that typically lie with 0 to 4000 cm^{-1}.[18] The higher-frequency vibrations, such as amide I (~1650 cm^{-1}, C=O stretching) and amide III (~1300 cm^{-1}, $C_\alpha H$/NH bending and CN stretching), have been discussed extensively.[19] However, the low-frequency part below 800 cm^{-1} has often been omitted or ignored, because of problems in the measurement and interpretation. More recent works suggest that the low-frequency vibrations sometimes provide ROA intensities comparable to those in the higher frequency region.[20,21] For example, bovine α-lactalbumin shows positive ROA signals at 133 and 168 cm^{-1}. Lately, similar bands at 73 and 125 cm^{-1} were observed in α-helical α-synuclein.[22] DFT simulation well reproduced the experimental peaks, but their analysis was difficult owing to delocalized and complicated protein vibrational motions.[20,21]

Only the latest instrumental advances, such as the availability of sharp notch/edge filters with cut-off frequency down to ~60 cm^{-1} make it possible to systematically explore this region by ROA. The low-frequency vibrational modes of polyamides have been studied using non-chiral Raman or far-infrared spectroscopy,[23–27] and the modes around 100 cm^{-1}

[a] *Department of Chemistry, Graduate School of Science, Osaka University, Osaka 560-0043, Japan. E-mail: aporoa@gmail.com*
[b] *Institute of Organic Chemistry and Biochemistry, Academy of Sciences, Flemingovo náměstí 2, 16610 Prague, Czech Republic. E-mail: bour@uochb.cas.cz*

† Electronic supplementary information (ESI) available. See DOI: 10.1039/d1cp04401j

have been assigned to amide groups connected by hydrogen-bonds. In general, the modes are delocalized and reflect higher-order structures of proteins or solute–solvent interactions. The possibility to detect long-range chirality of hydrogen-bonded amides by ROA thus appears appealing to analyze molecular flexibility, secondary and tertiary structures of proteins.

To understand better the low-frequency protein optical activity, we study a simple system, poly-L-alanine (PLA), which has been suggested as a good model for α-helices of proteins.[28–30] PLA is not soluble in water, but dissolves in dichloroacetic acid (DCA) where it adopts the α-helical conformation.[28–30] A theoretical study on α-helical $(Ala)_{10}$ predicted a strong ROA signal for a "breathing" mode of α-helix at 65 cm^{-1},[31] but it has not been experimentally observed so far. High-frequency ROA spectra of PLA at ~1300 cm^{-1} and similar peptides and proteins have already been linked to secondary structure and solution properties.[19,32,33]

Modern theoretical and computational methods allow one to link spectral shapes to the structure.[34,35] However, interpretation of the low-frequency region based on a reliable simulation is not known to us. We, therefore, introduce arbitrary helical coordinates, which make it easier to identify collective delocalized modes and assign the experimental bands. In the simulations, the solvent environment is accounted for by the dielectric localizable continuum model (CPCM)[36] as well as using "explicit" solvation based on clusters from molecular dynamics. The solvent stabilizes the α-helical geometry and contributes to the low-frequency signal, as shown for other molecular systems.[37–39] The MD-based solvent modeling is more advanced than the CPCM or static approach but also computationally more demanding because large molecular clusters and many MD geometries need to be calculated to obtain a converged spectrum.[40] In addition to the helical coordinates, intermolecular ones are used to describing vibrations among the PLA and solvent molecules in the first solvation sphere.[41]

We find that the observed strong ROA bands could be linked to the protein structure as the motion comprises relatively well-defined helical deformations. We hope that our observations will open a way for utilizing low-frequency ROA in studies of the higher-order chiral structures of proteins, such as fluctuated secondary structures and protein–protein interactions.

Materials and methods

Raman and ROA measurements

Raman and ROA spectra were measured on a homemade instrument (Osaka University) based on the design of Werner Hug.[13,14] The instrument is composed of an edge filter with a cut-off at ~60 cm^{-1} (US LPF, Iridian), a 532 nm continuous-wave DPSS laser (Ventus, Laser Quantum), a custom-made spectrometer (F/2.8), and a back-illuminated CCD detector (−70 °C, PIXIS400B, Princeton Instruments). Its scheme and further details are provided in Fig. S1 (ESI†). The quality of the instrument is documented in Fig. S2 (ESI†) on the enantiomers of neat 2-phenylpropionic acid (>98%, Tokyo Chemical Industry), providing nearly "mirror image" spectra, even close to the filter cut-off at ~65 cm^{-1}. Similar results were obtained for limonene and α-pinene enantiomers. We also found it important to calibrate the relative sensitivity of the instrument using the NIST emission standard.[42] A variable sensitivity across the measured wavenumber range is often ignored in ROA literature; however, in our case, below 300 cm^{-1} the correction increased the relative intensity by up to ~1.5 times compared to the raw spectra. Even after the correction a residual intensity error smaller than 10% may still be present, originating from slight changes in position or angle of the sample cell.

Poly-L-alanine (PLA, average molecular weight 21400, Sigma-Aldrich) was kindly provided by Prof. Yukihiro Ozaki, Kwansei Gakuin University. The peptide was dissolved in dichloroacetic acid (DCA, ≥99%, Sigma-Aldrich) or deuterated one (DCA-d_2, 98%D, Medical Isotopes) to a concentration of 75 g L^{-1}, and about 30 μL of the solution was sealed in a homemade drum cell.[17] Laser power at the sample was 260 mW. To suppress fluorescence background from residual impurities in the peptide, the samples were left in laser irradiation for one day before the measurements. For comparison, an α-helical protein, human serum albumin (HSA, ≥99%, Sigma-Aldrich) was dissolved in 0.10 M acetic acid/sodium acetate buffer (final pH 5.9) at concentration of 100 g L^{-1} and ROA spectrum was measured with 330 mW laser power and total exposure time of 25 h. Partially unfolded HSA was prepared and measured in a similar manner but an aqueous solution of an anionic surfactant, sodium dodecyl sulfate[43] (SDS, ≥99.0%, Fujifilm Wako Pure Chemical, 110 g L^{-1}), was used as a solvent. Reproducibility of the spectra was checked by repeated measurements. Five-point adjacent averaging was applied to ROA.

Molecular dynamics

The average geometry, structure of the first solvation sphere, and flexibility of PLA dissolved in DCA were investigated by MD simulations with a model Ac-$(Ala)_{19}$-NHMe peptide (Fig. 1), within the Amber programs.[44] The peptide in an α-helical conformation, $(\phi, \psi) = (-46^\circ, -56^\circ)$, was placed at the center of a cubic box (80^3 $Å^3$) filled with DCA molecules. The system was optimized and equilibrated for 1 ns under *NVT* condition (300 K, 1 fs step, density 1.56 g mol^{-1}), followed by 10 ns run, using the Amber FF14sb (for PLA) and GAFF (for DCA) force fields.

Spectral simulations

Raman and ROA spectral properties of model fragments were calculated using the density functional theory as implemented in the Gaussian program.[45] The DFT computations were extended to large molecular systems using the Cartesian coordinate tensor transfer (CCT) method.[46–48] The solvent was modeled both as a dielectric continuum and with explicit DCA molecules of the first solvation sphere using MD snapshots. In the latter approach, MD clusters were also embedded in a dielectrics.

In the pure dielectric rigid model an Ac-$(Ala)_{18}$-NHMe (abbreviated as $(Ala)_{18}$) peptide was created with backbone

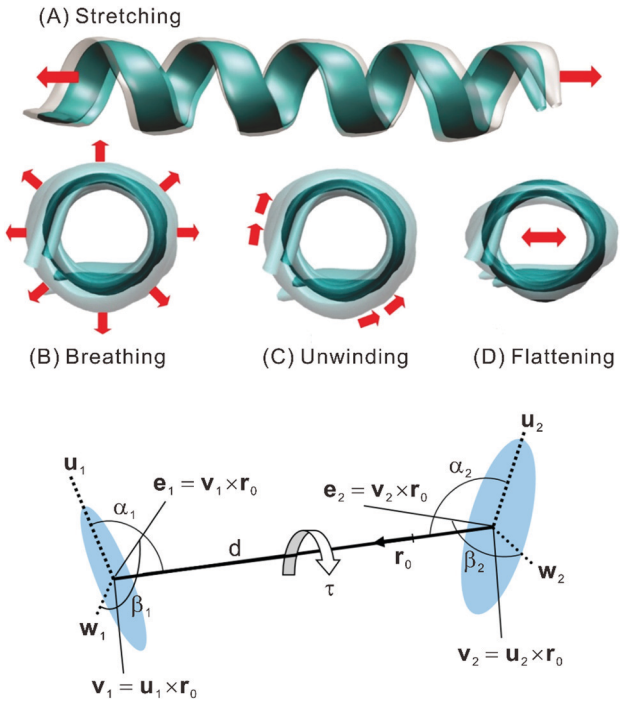

Fig. 1 Definition of the helical (top) and intermolecular (bottom) vibrational coordinates: (A) stretching mode of a helix defined as the biggest moment of inertia, $I_{xx} = \sum m_\lambda x_\lambda^2$, (B) breathing mode, sum of the secondary moments, $I_{yy} + I_{zz} = \sum_\lambda m_\lambda (y_\lambda^2 + z_\lambda^2)$, (C) unwinding mode, a sum of angular differences $\sum_\mu \sum_\lambda (\phi_\lambda - \phi_\mu)^2$, and (D) flattening mode, secondary moment difference, $I_{yy} - I_{zz} = \sum_\lambda m_\lambda (y_\lambda^2 - z_\lambda^2)$. Indices λ and μ run over all atoms forming the helix, m_λ are atomic masses, φ_λ are angles defining atomic positions projected in the yz plane perpendicular to the helical axis x. The coordinate system originates at the center of mass. The intermolecular coordinates consist of the distance of the mass centers (d), angles between the largest moments of inertia and the distance vector (α_1, α_2), rotation angles (β_1, β_2), and the torsion angle (τ). For the rotation angles, arbitrary vectors $\mathbf{e}_1$ and $\mathbf{e}_1$ were defined, using the largest (direction $\mathbf{u}_i$) and second-largest ($\mathbf{w}_i$) moments of inertia. Length of $\mathbf{u}_i$, $\mathbf{w}_i$, $\mathbf{v}_i$, $\mathbf{e}_i$, $\mathbf{r}_i$, and $\mathbf{r}_0$ is equal to one. Part of the figure is reprinted with permission from ref. 41. Copyright (2019) American Chemical Society.

torsional angles (ϕ, ψ) set to ($-66°$, $-44°$), typical for "hydrated" α-helices found in crystal structures of proteins.[49] A similar smaller fragment $(Ala)_{14}$ was partially optimized in the normal mode vibrational coordinates,[50,51] with fixed modes below 50 cm^{-1}. The Raman and ROA property tensors (α, G', A polarizability derivatives, harmonic force field) were calculated at the CAM-B3LYP[52]-GD3BJ[53]/6-31G** level of theory. Continuum solvent model (CPCM)[54] parameters of dichloroethane (DCE) were used to mimic DCA, as in a previous study.[33] From the fragments, the atomic tensors were transferred to $(Ala)_{18}$ using the CCTN program,[47] and Raman and ROA spectra were generated. Other theories (B3PW91[55]-GD2,[56] HF, BPW91, B3LYP) were also tested for comparisons, but in general, did not lead to better results.

In the MD approach, the spectra were calculated for 10 MD snapshots and averaged. DCA molecules farther than 5 Å from the peptide were deleted, and the spectra were simulated using $(Ala)_4$ or $(Ala)_6$ fragments capped with methyl residues and containing DCA molecules in the first solvation shell. The fragments were optimized with fixed normal modes within (100, −100) cm^{-1}, using the B3PW91-GD3BJ/6-31++G**/CPCM method for the former and B3PW91-GD3BJ/6-31G**/CPCM for the latter fragments. It appeared that the shorter fragments gave the worse results, despite the better basis set used, and were discarded. This confirms the limitations of the CCT method, where longer fragments are recommended for α-helices.[48,57] Finally, vibrational parameters were transferred from the fragments to the snapshot geometries to obtain the spectra.

Spectral intensities corresponding to the scattered circular polarization (SCP) backscattering experiment[1,2,58] were obtained for each vibrational mode i as

$$I_{i,\mathrm{Raman}} = 6\sum_{\beta=1}^{3}\sum_{\alpha=1}^{3}\left(\alpha_{i,\alpha\alpha}\alpha_{i,\beta\beta} + 7\alpha_{i,\alpha\beta}\alpha_{i,\alpha\beta}\right), \quad (1)$$

$$I_{i,\mathrm{ROA}} = 48\sum_{\beta=1}^{3}\sum_{\alpha=1}^{3}\left(3\alpha_{i,\alpha\beta}G'_{i,\beta\alpha} - \alpha_{i,\alpha\alpha}G'_{i,\beta\beta} + \sum_{\varepsilon=1}^{3}\sum_{\gamma=1}^{3}\varepsilon_{\alpha\beta\gamma}\alpha_{i,\alpha\varepsilon}A_{i,\beta\gamma\varepsilon}\right), \quad (2)$$

where α_i is the transition polarizability ($\alpha_i = \langle 0|\alpha|i\rangle$, similarly for G' and A, $|0\rangle$ and $|i\rangle$ is the ground and excited vibrational state, respectively). The α, G' and A polarizabilities are defined in ref. 1, $\varepsilon_{\alpha\beta\gamma}$ is the anti-symmetric tensor. Smooth spectra $S(\omega)$ were generated as,

$$S(\omega) = \sum_i I_i\left[1 - \exp\left(-\frac{\omega_i}{kT}\right)\right]^{-1}\left[4\left(\frac{\omega - \omega_i}{\Delta}\right)^2 + 1\right]^{-1}, \quad (3)$$

where ω_i is the vibrational frequency, k is the Boltzmann constant, T = 300 K is temperature, and Δ = 10 cm^{-1}. The normal mode displacements were visualized using the PLAY program.[59]

The definition of intermolecular coordinates has been adopted from ref. 41 and completed by four "helical" modes based on the moments of inertia defined in Fig. 1. Other intrinsic coordinates (distances, bond, and torsional angles and out-of-plane deformations) have been added automatically. For a quick assignment, we introduced an approximate potential energy distribution (PED)[60,61] using redundant internal vibrational coordinates (I). Based on a linear transformation to Cartesian coordinates (r), $I_i = B_{\lambda i} r_\lambda$, and a similar Cartesian-normal mode (Q) transformation, $Q_I = S_{\lambda I} r_\lambda$, normalized PED values were obtained using the PED program[62] as

$$\mathrm{PED}_{I,i} = \frac{A_{I,i}}{\sum_i A_{I,i}} \times 100\% \quad (4)$$

where $A_{I,i} = b_{I,i}^2 f_{ii} \omega_I^{-1}$ and $b_{I,i} = \sum_\lambda S_{\lambda I} B_{\lambda i}\sqrt{m_\lambda}$, m_λ denotes atomic masses, and f_{ij} are internal force constants.

Results and discussion

PLA molecular dynamics and α-helical geometry

The α-helical conformation appeared reasonably stable during the dynamics. In Fig. S3 (ESI†), the φ and ψ angles are recorded as sampled during the first 1 ns; the α-helical geometry did not change up to the end of the 10 ns simulation. We realize that this time is too short to explore the whole conformational space of the peptide. We use the dynamics only to have a model of PLA α-helix, estimate the dispersion of the (φ, ψ) angles in this conformation, and obtain a realistic configuration of DCA molecules in the first solvation sphere. As expected, the core residues (8–12) were the most rigid, the (φ, ψ) angles deviated from the average values ($-69°$, $-36°$) by less than $\sim 30°$. Only the N and C termini were frayed more. The average values are close to the standard α-helical angles of ($-66°$, $-44°$).[49] During the motion, the angles were often approaching values typical for 3_{10}-helix, ($-60°$, $-30°$); but on average only $\sim$16% of residues were closer to the 3_{10} values than to standard α-helical angles. Interestingly, only a relatively minor part ($\sim$10%) of DCA solvent molecules in the first solvation sphere formed hydrogen bonds to PLA, connecting COOH groups of DCA with amide PLA oxygens.

Experimental spectra

Experimental ROA and Raman spectra of α-helical PLA are shown in Fig. 2. The higher-frequency region (>800 cm^{-1}) is consistent with previous results.[32,33] For example, ROA bands at 1339, 1305, and 1279 cm^{-1} were assigned to the amide III vibrations. The amide I ROA bands appeared at $\sim$1600 cm^{-1}; they are weak and this is typical for α-helix as commonly observed for other homopolypeptides.[32] In addition, a positive ROA peak appears at 128 cm^{-1}, about 10 times stronger than the higher-frequency signals, accompanied by still relatively strong ROA peaks within 400–190 cm^{-1}. In the lowest-frequency region, solvents generally provide intense Raman bands, contributing to large photon-shot-noise in ROA spectra. However, the 128 cm^{-1} ROA band is still strong enough to be measurable, with intensity about 65 times bigger than the noise.

The signal strength enables a much shorter acquisition time as documented in Fig. 3, where the band could be detected already in 13 minutes. In this case the 128 cm^{-1} intensity is about 5 times bigger than the photon-shot-noise, and higher frequency bands are still buried in the noise. Further 1 h accumulation provided acceptable signal-to-noise ratio even for the other low-frequency bands (<500 cm^{-1}) (Fig. S4, ESI†). The long measurement time and low sensitivity is a notorious problem in ROA spectroscopy;[8] thus focusing on the low-frequency region facilitates many ROA applications on proteins.

As far as we know, such a strong chiral vibrational signal has not been observed for biopolymers, except for vibrational circular dichroism (VCD) signals of some fibrotic proteins where large VCD/IR ratios were detected.[63–66] In such cases, the proteins form nm–μm scale large aggregates of β-sheets, and the signal enhancement probably originates in a long-range order of amide chromophores.[67–69] On the other hand, the PLA low-frequency ROA signal in the present study is connected to the secondary structure of the ''isolated'' peptide and the signal originates from interactions within a few nm only, as discussed below.

PLA in the deuterated solvent DCA-d_2 exhibits low-frequency ROA spectrum similar to that in natural DCA (Fig. S5, ESI†). Below 700 cm^{-1}, the strength of ROA is maintained, with slight peak shifts of $\sim$8 cm^{-1}. Higher frequency bands shifted more, *e.g.* amide III signal at 1279 cm^{-1} disappeared in DCA-d_2. The shifts of a few cm^{-1} for the low-frequency bands were also predicted by the computations. This confirms that the model is realistic, but only indirectly indicates that the strong low-frequency ROA mainly comes from PLA itself. In DCA-d_2, also the PLA amides are deuterated; more exclusive isotopic substitutions, such as DCA-^{13}C, are too expensive for us. The band assignment, however, can be done easily *via* the

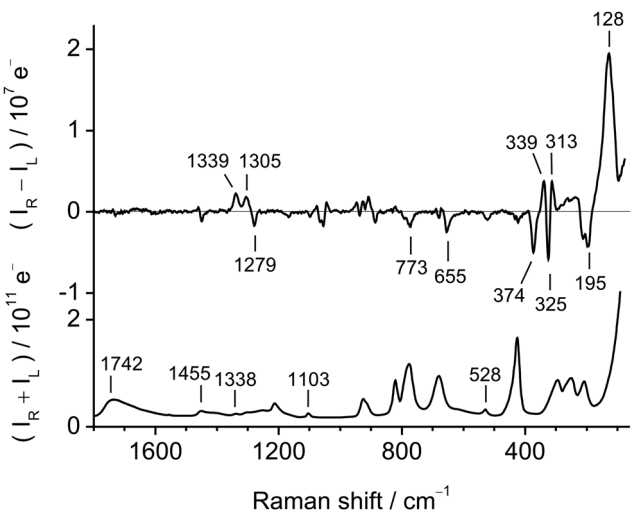

Fig. 2 Experimental ROA (top) and Raman (bottom, solvent spectrum is not subtracted) spectra of α-helical PLA dissolved in DCA at 25 °C with an exposure time of 13 h. Numbers in the Raman spectrum indicate PLA peaks, unlabeled bands are mostly from DCA.

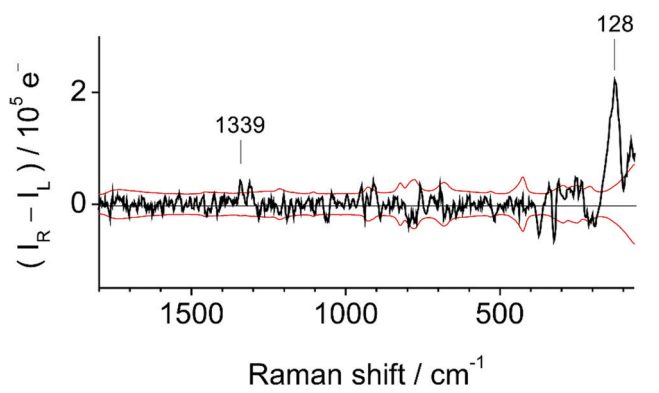

Fig. 3 ROA spectrum of α-helical PLA obtained with 13 min exposure time, other conditions were same as in Fig. 2, except for the relative intensity correction. The red curves indicate a level of the photon-shot-noise calculated from the corresponding Raman spectrum.

computations. For example, the model where the solvent was replaced by the CPCM continuum provided similar spectra to those based on MD clusters.

Raman spectrum of the PLA solution is dominated by solvent peaks (Fig. 2, bottom), which are virtually impossible to subtract (Fig. S6, ESI†). We can observe weakening of the carbonyl stretching band of DCA at 1676 cm^{-1} compared to pure DCA, which may indicate a significant hydrogen bonding of DCA to PLA. Probably, some ROA bands can be fully or partially attributed to the solvent (for example, the bands at 424, 679 and 774 cm^{-1}), as similar chirality transfer effects are relatively common in VOA spectroscopy.[70–72] However, the induced ROA intensity of DCA is supposed to be much smaller than that of PLA.

A similar low-frequency ROA spectral pattern was obtained for an α-helical protein, HSA (69% of α-helical content, PDB code, 1ao6). Its positive ROA band at 101 cm^{-1} is also 3–6 times stronger than the higher frequency modes, and is accompanied by a moderately intense negative band at 163 cm^{-1} (Fig. 4). The whole +/−/+ pattern of HSA at 226/163/101 cm^{-1} looks similar to that of PLA at 250/195/128 cm^{-1}. Despite the strong Raman band of solvent water, the signal-to-noise ratio of the 101 cm^{-1} ROA band of HSA is quite high, about 40. Previously, other α-helical proteins also exhibited similar +/−/+ ROA pattern and peak positions, *e.g.* α-lactalbumin at 289/168/133 cm^{-1} and hen and human lysozymes at 289/172/111 cm^{-1}.[20] This indicated that these bands may be used as convenient markers of protein α-helix, although low-frequency ROA of other secondary structures (β-sheet, β-hairpin, disordered) may also contribute.

The assignment of the low-frequency ROA signal to relatively rigid helices is confirmed by the partial unfolding of HSA. In the presence of SDS, the intensity of the ROA band of native HSA at 101 cm^{-1} decreases by 0.50-times. Also the "α-helical" amide III/I ROA bands at 1341/1667 cm^{-1} become 0.54/0.65-times smaller, indicating partial conversion of the α-helix to unfolded structure. ROA bands at 226/163 cm^{-1} also decrease, 0.32/0.57 times, although these might be affected by a small baseline drift apparent below 800 cm^{-1}. Nevertheless, these changes are consistent with the assignment of the ROA bands at 226/163/101 cm^{-1} to the α-helical structure. In Raman, the unfolding is most visible in the large intensity loss below 300 cm^{-1} and a weakening of the amide III bands at ~1300 cm^{-1}.

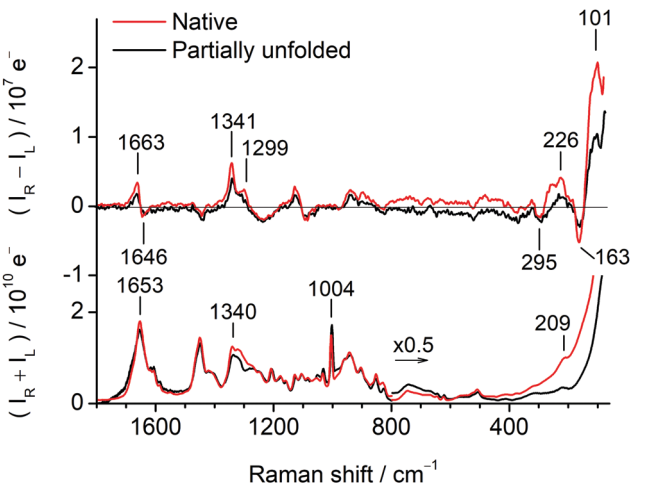

Fig. 4 Experimental ROA (top) and Raman (bottom) spectra of native HSA (red lines, shifts indicated) and partially unfolded one (black lines). Solvent background was subtracted from the Raman spectra.

Simulated PLA spectra

The calculations are compared to the experimental ROA spectrum in Fig. 5. A reasonable agreement with the experiment can already be seen for the two static CPCM models (CPCM 1 and 2), where different functionals (CAM-B3LYP-GD3BJ *vs.* B3PW91) and fragment lengths ($(Ala)_N$, N = 14 *vs.* 6) give quite similar spectral patterns. However, the CPCM1 model with the longer fragment gave peak frequencies closer to the experiment. For example, the experimental strongest positive peak at 128 cm^{-1} is calculated at 121 cm^{-1} and the experimental −/+/−/+ pattern at 374/339/325/313 cm^{-1} well corresponds to 372/341/320/304 cm^{-1} in the CPCM1 calculation. The relative intensities are also well-reproduced, although the bandwidth of

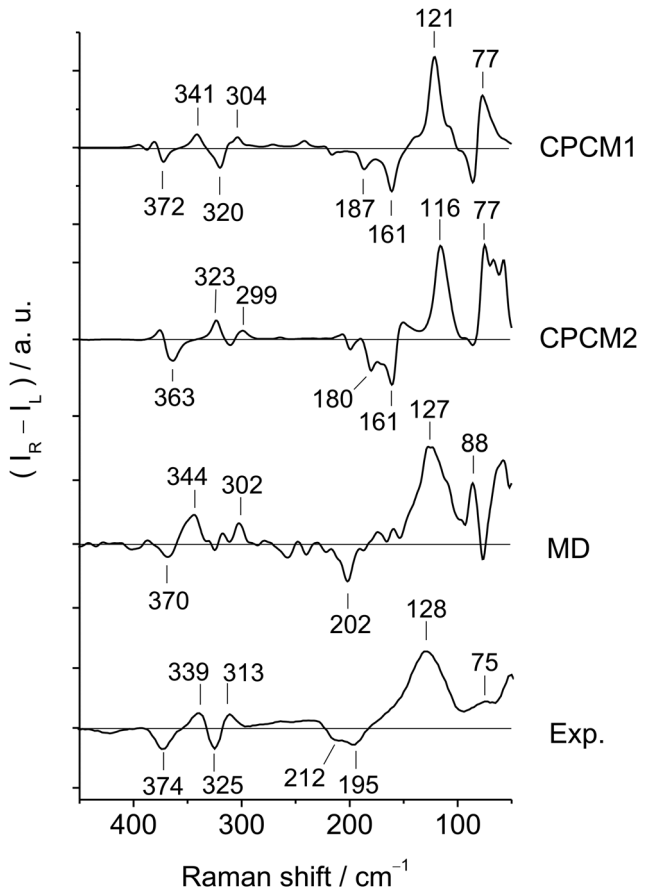

Fig. 5 Low-frequency ROA of PLA, the static $(Ala)_{18}$ CAM-B3LYP-GD3BJ/6-31G**/CPCM(DCE) (CPCM1) and B3PW91-GD3BJ (CPCM2) models, averaged spectrum obtained from the snapshots (MD), and the experiment. In the experiment, the lowest 90–50 cm^{-1} part may be slightly distorted by instrumental artifacts.

the calculated 121 cm^{-1} peak is too narrow. As discussed below, the length of the fragment $(Ala)_{14}$ in the CPCM1 is important to reproduce the low-frequency ROA spectrum. The calculated negative bands at 187 and 161 cm^{-1} probably correspond to 212 and 195 cm^{-1} in the experiment, although the frequency error is much bigger here, $\sim$30 cm^{-1}.

The modeling based on the clusters leads to several improvements (MD in Fig. 5). The main ROA band moves very close to the experimental value (127/128 cm^{-1} in MD/exp.) and the shape becomes broader and more realistic compared to the CPCM simulations (full width at half maximum: 33/39 cm^{-1} in MD/exp.). The experimental 195 cm^{-1} band is better reproduced by MD at 202 cm^{-1} than by CPCM at 161 cm^{-1}. On the other hand, MD intensities corresponding to the experimental 212 and 325 cm^{-1} bands are too weak. The observed band shifts and broadening in MD simulations, which are most apparent for the 128 cm^{-1} ROA band, reflect the flexibility of PLA in the solution phase. The structural deviation from the static model causes the peak broadening, however, the strong chirality at 128 cm^{-1} band is still preserved under the motion of α-helix. Below 90 cm^{-1}, the experimental spectrum may be partly distorted by an instrumental artifact; nevertheless also here the simulation seems to agree with it at least qualitatively.

Vibrational mode assignment

Based both on visual inspection of the normal modes and PED values, the low-frequency ROA bands are assigned to vibrational normal modes in Table 1. In particular, the 128 cm^{-1} ROA band is assigned to out-of-plane motions of the amide groups (mostly C═O), with a participation of the methyl groups. This more or less agrees with the previous assignment of polyamide Raman bands at $\sim$100 cm^{-1}, two types of vibrational motions of the amides with NH and O atoms moving perpendicularly or parallel to the amide plane.[23–27] Our computation indicates the ROA band is more specifically related to the perpendicular motion of the amides.

Character of the low-frequency modes

For the helical and intermolecular vibrational motions, histograms of potential energy distribution integrated over 10 cm^{-1} interval are plotted in Fig. 6a (an alternate representation can be found in Fig. S7, ESI†). The most prominent band positions are summarized in Table 1.

Interestingly, not only a helical mode seems to contribute significantly in the low-frequency region, but different helical coordinates dominate in different vibrations. The helical stretching is predicted to be very low, at $\sim$90 cm^{-1}, which would correspond to the so-called ''helical breathing'' mode at 65 cm^{-1} predicted for $(Ala)_{10}$ in a previous computational study.[31] The symmetric breathing of the helix supports two distinct vibration classes, around 180 and 320 cm^{-1}. Interestingly, the unwinding vibrations often dominate below 150 cm^{-1}. The flattening provides two distinct peaks only, around 200 and 90 cm^{-1}. Therefore, the experimental strongest ROA band of PLA at 128 cm^{-1} may be connected with the unwinding of α-helix. The atomic motions calculated for the static model (Fig. 6b) also support this unwinding nature, and the atomic movement around the helical axis is nicely visible.

A more detailed inspection of the normal mode displacement shows that the unwinding vibrations are not evenly spread over all $(Ala)_{18}$ residues, but consist of partially delocalized modes, for example comprising an $(Ala)_{12}$ segment. As a rule, the most delocalized helical modes provide the largest ROA signal, which is consistent with the previous study.[73] Local modes, such as CH_3 rotations ($\sim$266 cm^{-1}, Table 1), give very weak ROA intensity. The intermolecular modes occur within the lowest-frequency part of the spectrum ($<$100 cm^{-1}), thus partially overlapping with the helical stretching mode, but the contribution quickly diminishes above 125 cm^{-1}. The low-frequency vibrations are thus less-defined in terms of local vibrational coordinates (bonds, angles) or chemical groups (*e.g.* C═O stretching) and provide broader bands compared to the higher-frequency ones, but can still be partially classified by using the ''macroscopic'' helical and intermolecular coordinates. The ROA spectroscopy reveals their specificity, unseen with the unpolarized Raman technique.

In an alternate analysis, we decomposed the theoretical ROA intensity to amide, methyl, and chiral center groups (Fig. 7), by partial deletion of atomic polarizability derivatives.[21,25] The decomposition shows that the amide groups contribute to the strong ROA signal at 115 cm^{-1} (exp. 128 cm^{-1}) most, followed by the CH_3 groups. It is interesting that the contribution of the chiral centers $C_\alpha H$ is rather minor, *i.e.*, it is the helical

Table 1 Peak positions in cm^{-1} and assignments of ROA bands of PLA

Exp.	CPCM1[a]	MD[b]	Atomic motions	Intensity-carrying	Helical modes
75		88		All parts	Unwinding/stretching/flattening
128	121	127	oop (amide), CH_3	Amide (major), CH_3	Unwinding
195	161	202	Amide, CH_3	All parts	Flattening/breathing
212	187	216		All parts	
$\sim$240		239			
$\sim$270			CH_3 rotation		
313	304	302	CH_3 wag., amide	CH_3	
325	320		CH_3 wag., amide	CH_3	
339	341	344	CH_3 wag., amide	All parts	Breathing/flattening
374	372	370	ip (amide)	All parts	Flattening

[a] Static model at CAM-B3LYP-GD3BJ/6-31G**/CPCM(DCE). [b] MD-averaged. oop: out-of-plane deformation. ip: in-plane deformation.

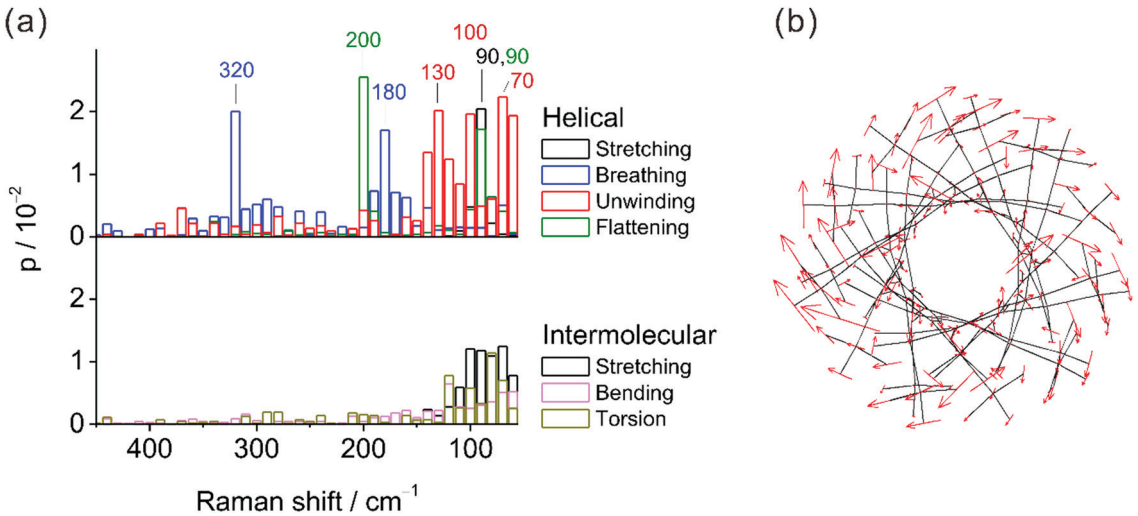

Fig. 6 (a) Relative potential energy distribution of the helical (top) and intermolecular (bottom) vibrational modes of PLA calculated for the MD clusters, and (b) atomic displacements related to the strong positive ROA band at 121 cm^{-1} in the CPCM1 calculation (128 cm^{-1} in the experiment).

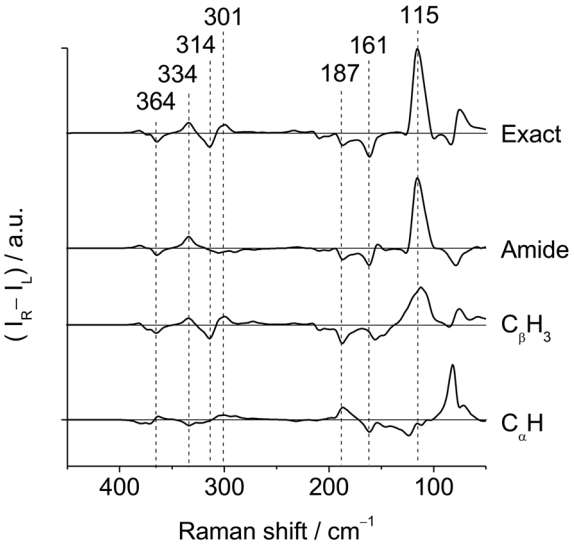

Fig. 7 Contribution of various molecular groups to ROA intensities calculated at the B3LYP/6-31G**/CPCM(DCE) level. From top to bottom, the exact result, contributions of the NHCO amides, side-chain methyl groups $C_\beta H_3$, and chiral carbon and its hydrogen $C_\alpha H$.

arrangements of the amide and methyl groups that lead to the strong chiral signals. The exceptional strength of the low-frequency ROA signals of PLA compared to those of the other α-helical proteins could be attributed to the abundance of methyl groups in PLA which are usually Raman active and partly contribute to the ROA bands. All molecular parts contribute to ROA within 400–150 cm^{-1}, except for the bands at 314 and 301 cm^{-1} governed by the CH_3 groups.

The delocalized nature of the low-frequency ROA bands can also be demonstrated by spectral simulations of $(Ala)_{18}$ with different fragment lengths, $(Ala)_N$ (N = 6–16), as shown in Fig. 8. By changing the length, we can estimate the effect of interactions between distant atoms on spectral intensities. For N = 18 all interactions are included. Significant spectral changes can be found below ~125 cm^{-1}, where ROA intensity at ~108 cm^{-1} grows up when N increases from 6 to 16. The peak position also moves from 101 cm^{-1} (N = 8) to 108 cm^{-1} (N = 16). A spectral convergence is achieved for N ~12, which corresponds to about 2 turns of the α-helix. The ~108 cm^{-1} band is not yet present for N = 6 (~one turn of the helix). On the other hand, the higher-frequency region converges faster, for example, a converged pattern in 400–300 cm^{-1} region is already provided by the $(Ala)_6$ fragment. Similarly, the short fragments were found sufficient to model the higher frequency vibrations above 1000 cm^{-1} in PLA[33] and the other peptides.[48] Because the interaction length reflected in the 128 cm^{-1} ROA band is about twice as long, the signal might be useful to analyze formation, flexibility or fluctuation of α-helical structures in solutions. To summarize the analysis, the strong ROA bands of PLA and other α-helical proteins at ~100 cm^{-1} thus mainly come from the unwinding motions of helically arranged amide groups and two and more turns of the helix are needed.

Conclusions

To understand low-frequency chirality of protein α-helices, we measured and analyzed ROA spectra of PLA and HSA down to ~65 cm^{-1}. Unusually strong positive ROA bands were observed both for PLA (at 128 cm^{-1}) and HSA (101 cm^{-1}). The signal strengths enabled us to measure the strongest ROA features within a few minutes, *i.e.*, in a much shorter time than normally required for such chiral measurements of proteins, which may boost ROA applications in structural analyses of proteins. The fragment-based DFT calculations were successfully applied to simulate the PLA spectrum, which revealed that the strong ROA signal at 128 cm^{-1} to a large part comes from an unwinding delocalized motion of α-helix, with an effective interaction length

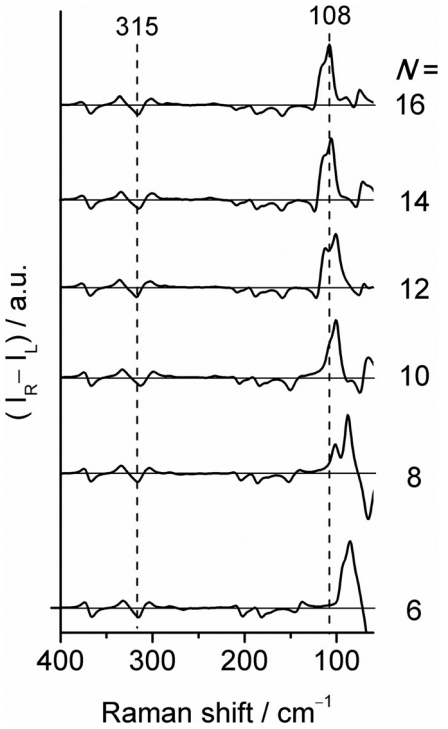

Fig. 8 Dependence of calculated ROA spectrum of α-helical $(Ala)_{18}$ on the fragment length $(Ala)_N$, as calculated at the B3LYP/6-31G** level of theory.

of about 12 amino acids (~2 turns of α-helix), including out-of-plane vibrations of hydrogen-bonded amides. Helical and intermolecular coordinates have been introduced to analyze the spectral pattern in terms of vibrational potential energy distributions and appeared extremely useful for the description and understanding of the low-frequency modes. MD combined with DFT provided the more realistic ROA spectrum compared to the static CPCM simulations. Intensity decompositions clarified that chiral arrangements of the amide and methyl groups in α-helical PLA provides the strong ROA signal and that local chirality in the vicinity of the $C_\alpha H$ groups plays a minor role. Because of the strength and tight link to the structure, the low-frequency ROA region may become a useful tool for protein structure studies.

Conflicts of interest

There are no conflicts to declare.

Acknowledgements

PLA solution was prepared by MSc Fumiya Kimura in Osaka University. This work was supported by JSPS KAKENHI (JP19K05524) and Shimadzu Science Foundation (to S. Y.) and the Czech Grant Agency (20-10144S, to P. B.) and Ministry of Education (LTC17012/CZ.02.1.01/0.0/0.0/16_019/0000729, to P. B.)

References

1 L. D. Barron, *Molecular Light Scattering and Optical Activity*, Cambridge University Press, Cambridge, 2004.
2 L. A. Nafie, *Vibrational Optical Activity*, John Wiley & Sons, Ltd, Chichester, UK, 2011.
3 J. Haesler, I. Schindelholz, E. Riguet, C. G. Bochet and W. Hug, *Nature*, 2007, **446**, 526–529.
4 P. Pančoška, E. Bitto, V. Janota and T. A. Keiderling, *Faraday Discuss.*, 1994, **99**, 287.
5 J. R. Cheeseman, M. S. Shaik, P. L. A. Popelier and E. W. Blanch, *J. Am. Chem. Soc.*, 2011, **133**, 4991–4997.
6 E. Blanch, *Methods*, 2003, **29**, 196–209.
7 T. Xiang, D. J. Goss and M. Diem, *Biophys. J.*, 1993, **65**, 1255–1261.
8 M. Krupová, J. Kessler and P. Bouř, *ChemPlusChem*, 2020, **85**, 561–575.
9 G. Holzwarth, E. C. Hsu, H. S. Mosher, T. R. Faulkner and A. Moscowitz, *J. Am. Chem. Soc.*, 1974, **96**, 251–252.
10 L. D. Barron, M. P. Bogaard and A. D. Buckingham, *J. Am. Chem. Soc.*, 1973, **95**, 603–605.
11 S. O. Pour, S. E. J. Bell and E. W. Blanch, *Chem. Commun.*, 2011, **47**, 4754.
12 M. Das, D. Gangopadhyay, J. Šebestík, L. Habartová, P. Michal, J. Kapitán and P. Bouř, *Chem. Commun.*, 2021, **57**, 6388–6391.
13 W. Hug and G. Hangartner, *J. Raman Spectrosc.*, 1999, **30**, 841–852.
14 W. Hug, *Appl. Spectrosc.*, 2003, **57**, 1–13.
15 K. Hiramatsu, H. Kano and T. Nagata, *Opt. Express*, 2013, **21**, 13515–13521.
16 X. Cao, R. K. Dukor and L. A. Nafie, *Theor. Chem. Acc.*, 2008, **119**, 69–79.
17 S. Yamamoto and H. Watarai, *J. Raman Spectrosc.*, 2010, **41**, 1664–1669.
18 G. Herzberg, *Molecular Spectra and Molecular Structure*, D. Van Nostrand Company Inc., Princeton, New Jersey, 1945.
19 L. D. Barron, L. Hecht, E. W. Blanch and A. F. Bell, *Prog. Biophys. Mol. Biol.*, 2000, **73**, 1–49.
20 J. Kessler, J. Kapitán and P. Bouř, *J. Phys. Chem. Lett.*, 2015, **6**, 3314–3319.
21 S. Yamamoto, J. Kaminský and P. Bouř, *Anal. Chem.*, 2012, **84**, 2440–2451.
22 A. Kurochka, J. Průša, J. Kessler, J. Kapitán and P. Bouř, *Phys. Chem. Chem. Phys.*, 2021, **23**, 16635–16645.
23 S. E. M. Colaianni and O. F. Nielsen, *J. Mol. Struct.*, 1995, **347**, 267–283.
24 O. Faurskov Nielsen, D. H. Christensen and O. Have Rasmussen, *J. Mol. Struct.*, 1991, **242**, 273–282.
25 S. Yamamoto, E. Ohnishi, H. Sato, H. Hoshina, D. Ishikawa and Y. Ozaki, *J. Phys. Chem. B*, 2019, **123**, 5368–5376.
26 H. Tadokoro, M. Kobayashi, H. Yoshidome, K. Tai and D. Makino, *J. Chem. Phys.*, 1968, **49**, 3359–3373.
27 G. Giraud, J. Karolin and K. Wynne, *Biophys. J.*, 2003, **85**, 1903–1913.
28 S.-H. Lee and S. Krimm, *J. Raman Spectrosc.*, 1998, **29**, 73–80.
29 M. Goodman, F. Toda and N. Ueyama, *Proc. Natl. Acad. Sci. U. S. A.*, 1973, **70**, 331–333.

30 A. Shoji, T. Kawai and A. Nishioka, *Makromol. Chem.*, 1978, **179**, 611–624.
31 C. Herrmann, K. Ruud and M. Reiher, *ChemPhysChem*, 2006, **7**, 2189–2196.
32 I. H. McColl, E. W. Blanch, L. Hecht and L. D. Barron, *J. Am. Chem. Soc.*, 2004, **126**, 8181–8188.
33 S. Yamamoto, T. Furukawa, P. Bouř and Y. Ozaki, *J. Phys. Chem. A*, 2014, **118**, 3655–3662.
34 K. Ruud, T. Helgaker and P. Bouř, *J. Phys. Chem. A*, 2002, **106**, 7448–7455.
35 V. Liégeois, K. Ruud and B. Champagne, *J. Chem. Phys.*, 2007, **127**, 204105.
36 J. Tomasi, B. Mennucci and R. Cammi, *Chem. Rev.*, 2005, **105**, 2999–3094.
37 J. Kapitán, V. Baumruk and P. Bouř, *J. Am. Chem. Soc.*, 2006, **128**, 2438–2443.
38 K. H. Hopmann, K. Ruud, M. Pecul, A. Kudelski, M. Dračínský and P. Bouř, *J. Phys. Chem. B*, 2011, **115**, 4128–4137.
39 F. Zielinski, S. T. Mutter, C. Johannessen, E. W. Blanch and P. L. A. Popelier, *Phys. Chem. Chem. Phys.*, 2015, **17**, 21799–21809.
40 J. Kessler, M. Dračínský and P. Bouř, *J. Comput. Chem.*, 2013, **34**, 366–371.
41 P. Michal, R. Čelechovský, M. Dudka, J. Kapitán, M. Vůjtek, M. Berešová, J. Šebestík, K. Thangavel and P. Bouř, *J. Phys. Chem. B*, 2019, **123**, 2147–2156.
42 V. Profant, M. Pazderková, T. Pazderka, P. Maloň and V. Baumruk, *J. Raman Spectrosc.*, 2014, **45**, 603–609.
43 S. Ghosh, S. Chakrabarty, D. Bhowmik, G. S. Kumar and N. Chattopadhyay, *J. Phys. Chem. B*, 2015, **119**, 2090–2102.
44 N. Kamiya, Y. S. Watanabe, S. Ono and J. Higo, *Chem. Phys. Lett.*, 2005, **401**, 312–317.
45 M. J. Frisch, G. W. Trucks, H. B. Schlegel, G. E. Scuseria, M. A. Robb, J. R. Cheeseman, G. Scalmani, V. Barone, G. A. Petersson, H. Nakatsuji, X. Li, M. Caricato, A. V. Marenich, J. Bloino, B. G. Janesko, R. Gomperts, B. Mennucci, H. P. Hratchian, J. V. Ortiz, A. F. Izmaylov, J. L. Sonnenberg, D. Williams-Young, F. Ding, F. Lipparini, F. Egidi, J. Goings, B. Peng, A. Petrone, T. Henderson, D. Ranasinghe, V. G. Zakrzewski, J. Gao, N. Rega, G. Zheng, W. Liang, M. Hada, M. Ehara, K. Toyota, R. Fukuda, J. Hasegawa, M. Ishida, T. Nakajima, Y. Honda, O. Kitao, H. Nakai, T. Vreven, K. Throssell, J. A. Montgomery Jr., J. E. Peralta, F. Ogliaro, M. J. Bearpark, J. J. Heyd, E. N. Brothers, K. N. Kudin, V. N. Staroverov, T. A. Keith, R. Kobayashi, J. Normand, K. Raghavachari, A. P. Rendell, J. C. Burant, S. S. Iyengar, J. Tomasi, M. Cossi, J. M. Millam, M. Klene, C. Adamo, R. Cammi, J. W. Ochterski, R. L. Martin, K. Morokuma, O. Farkas, J. B. Foresman and D. J. Fox, *Gaussian 16 Rev. A.03*, Gaussian, Inc., Wallingford, CT, 2016.
46 S. Yamamoto and P. Bouř, in *Frontiers of Quantum Chemistry*, ed. M. J. Wójcik, H. Nakatsuji, B. Kirtman and Y. Ozaki, Springer Singapore, Singapore, 2018, pp. 181–197.
47 P. Bouř, J. Sopková, L. Bednárová, P. Maloň and T. A. Keiderling, *J. Comput. Chem.*, 1997, **18**, 646–659.
48 S. Yamamoto, X. Li, K. Ruud and P. Bouř, *J. Chem. Theory Comput.*, 2012, **8**, 977–985.
49 T. Blundell, D. Barlow, N. Borkakoti and J. Thornton, *Nature*, 1983, **306**, 281–283.
50 P. Bouř and T. A. Keiderling, *J. Chem. Phys.*, 2002, **117**, 4126–4132.
51 J. Hudecová, K. H. Hopmann and P. Bouř, *J. Phys. Chem. B*, 2012, **116**, 336–342.
52 T. Yanai, D. P. Tew and N. C. Handy, *Chem. Phys. Lett.*, 2004, **393**, 51–57.
53 S. Grimme, S. Ehrlich and L. Goerigk, *J. Comput. Chem.*, 2011, **32**, 1456–1465.
54 V. Barone and M. Cossi, *J. Phys. Chem. A*, 1998, **102**, 1995–2001.
55 J. P. Perdew, K. Burke and Y. Wang, *Phys. Rev. B: Condens. Matter Mater. Phys.*, 1996, **54**, 16533–16539.
56 S. Grimme, *J. Comput. Chem.*, 2006, **27**, 1787–1799.
57 N. S. Bieler, M. P. Haag, C. R. Jacob and M. Reiher, *J. Chem. Theory Comput.*, 2011, **7**, 1867–1881.
58 P. L. Polavarapu, *Vibrational spectra: principles and applications with emphasis on optical activity*, Elsevier, Amsterdam, 1998, vol. 85.
59 P. Bouř, *PLAY*, Academy of Sciences, Prague, 1995.
60 E. B. Wilson, *J. Chem. Phys.*, 1939, **7**, 1047–1052.
61 T. Shimanouchi, M. Tsuboi and T. Miyazawa, *J. Chem. Phys.*, 1961, **35**, 1597–1612.
62 P. Bouř, *PED*, Academy of Sciences, Prague, 2020.
63 S. Ma, X. Cao, M. Mak, A. Sadik, C. Walkner, T. B. Freedman, I. Lednev, R. Dukor and L. A. Nafie, *J. Am. Chem. Soc.*, 2007, **129**, 12364–12365.
64 A. Fulara, A. Lakhani, S. Wójcik, H. Nieznańska, T. A. Keiderling and W. Dzwolak, *J. Phys. Chem. B*, 2011, **115**, 11010–11016.
65 D. Kurouski, R. K. Dukor, X. Lu, L. A. Nafie and I. K. Lednev, *Biophys. J.*, 2012, **103**, 522–531.
66 M. Pazderková, T. Pazderka, M. Shanmugasundaram, R. K. Dukor, I. K. Lednev and L. A. Nafie, *Chirality*, 2017, **29**, 469–475.
67 T. J. Measey and R. Schweitzer-Stenner, *J. Am. Chem. Soc.*, 2011, **133**, 1066–1076.
68 W. R. W. Welch, J. Kubelka and T. A. Keiderling, *J. Phys. Chem. B*, 2013, **117**, 10343–10358.
69 J. Průša and P. Bouř, *Chirality*, 2018, **30**, 55–64.
70 J. Sadlej, J. C. Dobrowolski and J. E. Rode, *Chem. Soc. Rev.*, 2010, **39**, 1478–1488.
71 M. Losada and Y. Xu, *Phys. Chem. Chem. Phys.*, 2007, **9**, 3127.
72 J. Šebestík, F. Teplý, I. Císařová, J. Vávra, D. Koval and P. Bouř, *Chem. Commun.*, 2016, **52**, 6257–6260.
73 V. Profant, V. Baumruk, X. Li, M. Šafařík and P. Bouř, *J. Phys. Chem. B*, 2011, **115**, 15079–15089.